NIFS--48

JP9107010

Application of Intermediate Frequency Range Fast Wave to JIPP T-IIU Plasma

T. Seki, R. Kumazawa, Y. Takase, A. Fukuyama, T. Watari, A. Ando, Y. Oka, O. Kaneko, K. Adati, R. Akiyama, R. Ando, T. Aoki, Y. Hamada, S. Hidekuma, S. Hirokura, K. Ida, K. Itoh, S.-I. Itoh, E. Kako, A. Karita, K. Kawahata, T. Kawamoto, Y. Kawasumi, S. Kitagawa, Y. Kitoh, M. Kojima, T. Kuroda, K. Masai, S. Morita, K. Narihara, Y. Ogawa, K. Ohkubo, S. Okajima, T. Ozaki, M. Sakamoto, M. Sasao, K. Sato, K.N. Sato, F. Shinbo, H. Takahashi, S. Tanahashi, Y. Taniguchi, K. Toi and T. Tsuzuki

(Received – Sep. 3, 1990)

NIFS-48 Sep. 1990

APPLICATION OF INTERMEDIATE FREQUENCY RANGE FAST WAVE TO JIPP T-IIU PLASMA

T. SEKI, R. KUMAZAWA, Y. TAKASE*, A. FUKUYAMA**, T. WATARI, A. ANDO, Y. OKA, O. KANEKO, K. ADATI, R. AKIYAMA, R. ANDO, T. AOKI, Y. HAMADA, S. HIDEKUMA, S. HIROKURA, K. IDA, K. ITOH, S.-I. ITOH, E. KAKO, A. KARITA, K. KAWAHATA, T. KAWAMOTO, Y. KAWASUMI, S. KITAGAWA, Y. KITOH, M. KOJIMA, T. KURODA, K. MASAI, S. MORITA, K. NARIHARA, Y. OGAWA, K. OHKUBO, S. OKAJIMA***, T. OZAKI, M. SAKAMOTO, M. SASAO, K. SATO, K.N. SATO, F. SHINBO, H. TAKAHASHI, S. TANAHASHI, Y. TANIGUCHI, K. TOI, T. TSUZUKI

National Institute for Fusion Science, Nagoya 464-01, Japan

*Massachusetts Institute of Technology, Cambridge,Massachusetts, U.S.A

**School of Engineering, Okayama University, Okayama 700, Japan

***Department of Applied Physics, Chubu University, Kasugai 487, Japan

ABSTRACT

A series of experiments using a newly constructed 130 MHz RF system has been conducted on the JIPP T-IIU tokamak since 1989. It is predicted theoretically that the fast wave in this range of frequency weakly interacts with particles. Though weak, two mechanisms of wave absorption were identified in the experiment: electron Landau/transit-time damping and 3rd ion cyclotron harmonic heating. The former has an intimate connection with fast wave current drive and the latter can

provide a new regime of plasma heating or a possible method of controling transport of α-particles. It was found that the efficiency of the 3rd cyclotron heating is improved by using it in the combination with NBI and ICRF heating. The heating efficiency obtained is as high as that of conventional heating. The experimental results are also analyzed on the basis of a theory of the global wave which takes into account wave particle interactions. These mechanism of wave particle interactions are competing with each other as they will be under more realistic reactor conditions.

"Keywords" fast wave current drive, electron heating, 3rd ion harmonic heating, 130 MHz rf system, antenna phasing, JIPP T-IIU tokamak

I. INTRODUCTION

The intermediate range of frequency extending from 3rd ion cyclotron harmonic frequency to lower hybrid frequency is important in the developmental study of nuclear fusion. First, this frequency range is suitable for fast wave current drive. At present, only the lower hybrid current drive (LHCD) is an experimentally established scheme for steady operation of tokamaks. However, recent experiments of LHCD reveal the exsistence of a density limit beyond which current drive fails. This is associated with the wave accessibility of the slow wave[1,2]. In a high electron temperature plasma where the damping length of the slow wave is shorter than the plasma

radius, LHCD does not work efficiently in the plasma core region[3]. From these points of view, fast wave current drive (FWCD) has been proposed[4-9] as an alternative scheme. There are some experimental contributions in this field done by ourselves[10-14] and by others[15-18]. FWCD utilizes compressional Alfven waves. Since this wave has weak electric field, the wave damping length tends to be much larger than the dimension of a plasma in present day tokamaks. For this reason it has not been very easy to get a clear demonstration of fast wave current drive.

On the other hand, it has been long since the second harmonic heating was shown to be a possible heating scheme[19]. Since then, it has been examined in several devices[20-22]. However, few experimental results are available for frequencies with harmonic number larger than 2. The higher harmonic ion cyclotron damping mechanism is related to finite Larmor radius effects and is expected to be enhanced as plasma parameters are improved. In a near future plasma, the 3rd cyclotron harmonic damping may become strong enough for plasma heating. As discussed by Stix[23], higher harmonic heating exhibits a runaway behavior as analyzed in the Fokker-Planck equation. This nature will be utilized in producing high energy ion tail so that the fusion reaction rate is enhanced and a high Q-value is obtained.

As discussed in ITER design activities, the wave absorption by ions may hinder fast wave from being a good current driver; it has been warned by theorists[8,9] that electron and ion wave absorption mechanisms are in competition. This is particularly

true when α-particles exist even as a small percentage of ions and quite unfavorable in view of current drive. However, at the same time, this means that there is a possibility that fast wave can be used as a method of α-particle control.

In spite of such potential usefulness, few experiments have addressed this important frequency range. We recently constructed a 130 MHz RF system in order to assess various wave absorption mechanisms and to get insight into the problems we will encounter in future applications to devices of more reactor relevance. This paper reports the first results from experiments conducted using the newly installed equipment. The experimental setup used in the experiment is explained in section II. The experimental results are presented in section III. Subsection (a) deals with electron heating which is a dominant heating mechanism in the low density regime. Subsection (b) deals with ion heating, which dominates in the high density regime particulary in the presence of high energy ions. These two mechanisms are competitive as predicted by the theory. In section IV, the experimental results are analyzed by the use of a computer simulation code, and implications are discussed. Finally, the results are summarized and conclusions are presented in section V.

II. EXPERIMENTAL SETUP

The JIPP T-IIU tokamak is a device which has a major radius of 0.91 m and a minor radius of 0.23 m. Toroidal magnetic field can be raised up to 3 tesla. 10 % - hydrogen mixed deuterium gas

is used in the experiment. As shown in Fig.1, there are eight antennas installed on the high field side of the vacuum chamber. Four of them make an 130 MHz antenna array aligned in toroidal direction. The same antennas have been used in 40 MHz ICRF heating experiments[24,25]. Since the wavelength of 130 MHz is shorter than that of 40 MHz, the antennas were shortened for their poloidal length to be less than a quarter wavelength. The wave is thereby radiated from the high field side around the equatorial plane. These 4 antennas are impedance matched by double stub tuners and connected to a power oscillator. The oscillator has two outputs which are further doubled into four by use of two power dividers. The phase angles are varied by changing the length of the matched section. Prior to the experiment, the total system is tuned for one of the available four phasings: $(0,0,0,0)$, $(0,\pi,0,\pi)$, $(0,\pi/2,\pi,3\pi/2)$, and $(0,-\pi/2,-\pi,-3\pi/2)$. When toroidal magnetic field is 3 T, 130 MHz corresponds to 3rd ion cyclotron harmonics of hydrogen (6th harmonics of deuterium). The maximum power is 750 kW, where power refers to the net power injected into the plasma throughout this paper.

The other antennas are used as 40 MHz ICRF heating antennas as they have been in the past [24,25]. The plasma is heated in a two-ion hybrid heating regime with a maximum power of 500 kW. Also, a hydrogen beam of 30 keV is injected tangentially(NBI) with a maximum input power of 300 kW. They are used as auxiliaries in the present experiment in order to bring the plasma parameters into a proper range.

III. EXPERIMENTAL RESULTS

(a) ELECTRON HEATING

In previous papers we have visited fast wave current drive with frequencies of 40 MHz[10] and 800 MHz[11-13]. In the latter experiment a clear reduction of the loop voltage was observed as we launched FW. However, drop of the loop voltage turned out to be significant at plasma densities $< 1\times10^{19}$ m^{-3} which are not much higher than the LHCD density limit. This might be due to mode conversion of the wave to slow wave[8] or to insufficient power being applied. The power available was limited to 70 kW. In high current discharges, however, we observed an enhancement in soft X-ray emission at a density to some extent higher than the LHCD limit, which indicates, at least, an interaction of the fast wave with electrons[13]. On the other hand, in the experiment with 40 MHz[10] we were able to drive a current in a density range much higher than the LHCD density limit. In this experiment, we stressed the FWCD regime where frequency is low enough to exclude the lower hybrid resonance layer inside the plasma. However, the electron temperature of the target plasma was low, and we failed to give a convincing explanation for the so-called spectrum gap filling problem.

In the present experiment the power is higher than that used in the 800 MHz experiment. The net power input depend on the density of the target plasma and we can inject 200 kW even with low density of plasma. The central electron temperature is 1 ~ 1.5 keV with the plasma current 200 kA, which is much higher than that in the 40 MHz experiment. With this new experimental

setup, we searched for the condition where wave interacts with electrons. In a survey changing the plasma density we reconfirmed the presence of a regime where electron heating dominates. A typical shot is shown in Fig.2: the ECE signal shown in (a) stands for central electron temperature without distortion of electron distribution function. The ECE signal rises when RF pulse is applied, and it decreases gradually in association with the increase of the plasma density(see (c)). On the JIPP T-IIU, the density usually increases when RF is applied. This is because a lot of carbon tiles are used and carbonization has been done in other confinement studies[24]. We have applied Ti-gettering in order to reduce recycling and we are able to reduce the density of the target plasma down to 0.8×10^{19} m^{-3}. As shown in Fig.2(a), the enhancement of the ECE signal is observed for the plasma in the density range lower than 2×10^{19} m^{-3}. The fluctuation at the top of the RF pulse shown in Fig.2(a) reflects the presence of toroidal eigen modes. The loop voltage increases for a short time span just after the application of RF and then begins to decrease. This transient behavior is associated partly with the imperfect performance of the I_P regulation circuitry and partly with the current profile change. We defined P_{Ohm} by

$$P_{Ohm} = V_L \cdot I_p - \frac{1}{2}\frac{\partial}{\partial t}(l_i \cdot I_p^2) \qquad (1)$$

and use it in place of V_L as an indicator of electron heating or current drive. Here, V_L is the loop voltage, I_P is the plasma

current, and l_i is the internal inductance. The broken line in Fig.2(d) is obtained by evaluating the P_{ohm} with fixed l_i. The solid line is obtained by taking into account dl_i/dt, which is deduced from the difference of the stored energies evaluated from diamagnetic signal and magnetic flux (Fig.2(b)). This P_{ohm} decreases with the rise of the electron temperature. The reduction of the P_{ohm} is observed most clearly at a power level of 200 kW. The decrement is smaller with less power. With a higher power, the impurities accumulate more rapidly and the plasma density rises more quickly. The drop of the loop voltage was not observed clearly in the previous experiment[13] in this density range. The improvement here may be attributed to the higher power used in the present experiment and to the appropriate choice of RF frequency. The interaction of the wave with electrons has been reported also from JFT-2M[16], where ECH was applied in order to produce seed electrons, which are predicted to be important with regard to the spectrum gap problem. Though ECH is not available on the JIPP T-IIU, high current density due to the relatively high B_t makes it possible to raise the electron temperature of the target plasma to a level comparable to that in JFT-2M with ECH. The electron heating observed in the low density regime in JIPP T-IIU, therefore, reconfirms the importance of the presence of the high energy electrons. In Fig.3, the spectra of the soft X-rays with RF and without RF are compared. We notice an enhancement in the X-rays in the energy range from 10 to 25 keV. X-rays of energies higher than 25 keV are counted in the highest pulse height as seen in Fig.3 because of saturated amplification. From these

observations it is found that the wave interact with electrons of energies higher than 10 keV. We examined 4 variations of phasing $(0,0,0,0)$, $(0,\pi,0,\pi)$, $(0,+\pi/2,+\pi,+3\pi/2)$, and $(0,-\pi/2,-\pi,-3\pi/2)$. The last two are particularly important because in these cases the excited wave has toroidal directionality and is related directly to current drive. However, the rise in the ECE signal and the drop in the loop voltage are obtained most clearly in this experiment with $(0,\pi,0,\pi)$ phasing. The spectrum of the excited wave with this phasing peaks around $n_{//} = 4.5$ which corresponds to an electron energy of about 20 keV.

The strength of the wave particle interaction is estimated in WKB approximation in terms of inverse damping length, $\gamma = L^{-1}$, defined as follows:

$$\gamma = \frac{\partial \log A}{\partial s} = \frac{\mathrm{Im}D}{\left|\frac{\partial D}{\partial \dot{k}}\right|} \qquad (2)$$

with

$$\left|\frac{\partial D}{\partial \dot{k}}\right| = \frac{c}{\omega} 2n_{perp}\left\{(\varepsilon_{xy} - n_{//}^2)^2 + n_{//}^2 n_{perp}^2\right\}^{1/2} \approx \left|\frac{c}{\omega} 2n_{perp}\varepsilon_{xx}\right| \qquad (3)$$

and

$$\mathrm{Im}\,D = \left(\varepsilon_{xx}\,\mathrm{Im}\,\varepsilon_{xx} + \frac{\mathrm{Im}\,\varepsilon_{zz}}{\varepsilon_{zz}^2} n_{perp}^2 n_{//}^2 \frac{\varepsilon_{xy}\varepsilon_{yx}}{\varepsilon_{xx}} \right) \tag{4}$$

$$= \left\{ 2\pi^{1/2} \zeta_{e,0} \exp(-\zeta_{e,0}^2) \right\} \frac{\omega_{pe}^2}{\omega^2} \left(\varepsilon_{xx} k_{perp}^2 \rho_{e,perp}^2 \frac{T_{e,perp}}{T_{e,//}} + \frac{1}{2} \frac{\omega^2}{v_{e,//}^2 k_{//}^2} \frac{1}{\varepsilon_{zz}^2} n_{perp}^2 n_{//}^2 \left[\frac{\varepsilon_{xy}\varepsilon_{yx}}{\varepsilon_{xx}} \right] \right)$$

$$+ \pi^{1/2} \sum_{j=i,a} \frac{\omega_{pj}^2}{\omega^2} \sum_{n \geq 1} \exp(-\zeta_{j,n}^2) \left[\zeta_{j,0} - \left(1 - \frac{T_{j,perp}}{T_{j,//}} \right) \zeta_{j,n} \right] \frac{n^2}{2n!} \left(\frac{1}{2} k_{perp}^2 \rho_{j,perp}^2 \right)^{n-1} \varepsilon_{xx} ,$$

where A is the wave amplitude, ε with subscripts are the elements of dielectric tensor, ρ_e is the electron Larmor radius, ζ_0 is the phase velocity normalized to the thermal velocity of electrons, and ω_{pe} is the electron plasma frequency. The term with the factor $2\pi^{1/2}\zeta_{e,0}\exp(-\zeta_{e,0}^2)$ consists of two wave absorption mechanisms: the first term comes from the transit-time damping and the second term comes from the electron Landau damping. The other terms are contributions from various orders of higher harmonic ion cyclotron damping, for which the following approximate analytical expression can be used:

$$\bar{\gamma}_i = \frac{1}{2a} \sum_n \frac{\omega_{pi}^2}{\omega^2} k_{perp} \frac{1}{2} \frac{\pi\omega}{n \frac{d}{dx}[\omega_{ci}(x)]_{x=x_n}} \frac{n}{2(n-1)!} \left(\frac{1}{2} k_{perp}^2 \rho_{i,perp}^2(x_n) \right)^{n-1} \left| \frac{c}{\omega} 2 n_{perp} \varepsilon_{xx} \right|^{-1} . \tag{5}$$

where a is the plasma minor radius, ω_{pi} is the ion plasma frequency, ω_{ci} is the ion cyclotron frequency, ρ_i is the ion

Larmor radius, and x_{0n} is the location of the n-th ion cyclotron harmonic resonance. Eq.(4) is essentially the same as those obtained by Moreau et al.[5] and Chiu et al.[8] except for the ion damping term and the somewhat different ordering used.

In the intermediate frequency range, each damping mechanism is weak and competitive with the others. Substituting plasma parameters relevant to this heating regime we get the damping length, L, for the respective damping mechanisms: $L \sim 1.4 \times 10^5$ m for the transit-time damping, $L \sim 2.9 \times 10^3$ m for the electron Landau damping, and $L \sim 1.1 \times 10^6$ m for the 3rd cyclotron harmonic damping of hydrogen. Here we assume T_e to be 1.5 keV. These damping lengths are much larger than the toroidal length of the plama. These wave absorption mechanisms may not be strong enough, because some parasitic absorption of the wave is assumed to exist in an experimental situation. However, if we take into account a presence of high energy electron tail as suggested in Fig.3, we obtain $L \sim 8.9 \times 10^1$ m for the transit-time damping, and 2.1×10^3 m for electron Landau damping. Therefore, the substantial electron heating observed in the experiment is ascribed to the transit-time damping. We assumed here that $T_{e,//} \sim T_{e,perp}$ although it is likely that the distribution function of high energy tail electrons is slightly anisotropic with $T_{e,perp} < T_{e,//}$. As readily seen from Eq.(4), the ratio of the Landau damping to the transit-time damping is given by

$$\delta \sim \frac{1}{2}\left(\frac{m_e c^2}{T_{e,perp}}\frac{\omega^2}{\omega_{pe}^2}\right)\cdot\left(1-\left(\frac{\omega}{\omega_{ce}}\right)^2\right)^2 \sim 3.4 \times 10^{-2}. \qquad (6)$$

If we take into account the temperature anisotropy, the estimate given above may somewhat overestimate the transit-time damping.

Figure 4 shows the stored energy versus the plasma density, where filled circles are the data from discharges without RF and are subject to the neo-Alcator-like scaling as indicated by the solid line. The open circles are the data from discharges with RF; the stored energy increases only in the density range between 1×10^{19} ~ 3×10^{19} m^{-3}. This means that the electron heating does not work in the high density range and the higher harmonic ion cyclotron damping, the third term of Eq.(4), is not yet substantial.

Finally, the experimental conditions of the present experiment are mapped in Fig.5 together with those of other experiments dedicated to FWCD[6]. The abscissa is the predicted density limit[2] and the ordinate is the experimentally observed density. The solid line indicates that the observed density is equal there to the predicted density limit. In order to exclude the lower hybrid resonance layer from the plasma perfectly, the central density will have to be higher than the theoretical limit at least by one-order of magnitude. The data of the present experiment is labeled C, recording a density more than two orders of magnitude higher than the LHCD density limit. The density of the present experiment is also higher by one order of magnitude than that of our previous experiment, labeled B (40MHz).

(b) ION HEATING

In the present experiment where Bt is set around 3 T, the

3rd cyclotron resonance layer of hydrogen (i.e. 6th harmonics of deuterium) ions falls on the center of the plasma. In the case of JIPP T-IIU with its aspect ratio of 4, the layers of 5th- and 7th- harmonics of deuterium ions also locate inside the plasma. The 3rd harmonics of the hydrogen is, however, assumed to be the primary wave absorption mechanism, because higher harmonic heating is associated with finite Larmor radius effect. Though several works[19-22] have successfully demonstrated the 2nd cyclotron heating, the 3rd cyclotron harmonic damping is weaker by one order of $(k_{perp} \cdot \rho)^2$ and there are fewer works devoted to it. Since $(k_{perp} \cdot \rho)^2$ scales with n_e, an increase in the plasma density enhances the damping in general. However, as seen in Fig.4, it is not yet so strong in the JIPP T-IIU plasma as to increase the stored energy significantly.

It was found in the experiment that the 3rd cyclotron heating mechanism becomes much stronger when 130 MHz RF is applied superposed on other means of ion heating. Figure 6 shows a time history of a typical shot. Additonal heatings are applied in the flat top phase of the plasma current(I_P - 230 kA), where the Ohmic input power, P_{Ohm}, is about 400 kW. As shown in (b), NBI power, P_{NBI}, and 40MHz ICRF power, P_{ICRF}, are applied with the proper time delays in order to observe their respective effects. Power levels are equal at around 300 kW. This is the target plasma of the 130 MHz RF heating and 130 MHz is applied with a power level of 400 KW in the last stage. One can notice that the stored energy obtained from diamagnetism increases in coincidences with the application of each different additional

heating. We pay particular attention in this paper to the fact that the stored energy increment due to 130 MHz has been clearly identified(see Fig.6(e)). The loop voltage drop seen in (a) at the time of NBI injection is due partly to the NBI current drive. Its drop on the application of ICRF(40 MHz) is due to electron heating; since two-ion hybrid heating is adopted in JIPP T-IIU, electron heating is the dominant wave absorption mechanism. The central electron temperature increases when 40 MHz RF power is injected, and is sustained during the 130 MHz RF power-applied phase as shown in (d). We also notice that neutron yield is markedly enhanced when 130 MHz RF power is injected as shown in (c).

On JIPP T-IIU, an application of RF power is followed in most cases by an electron density increase (see Fig.6(c)). Since the stored energy increases on the Alcator-scaling up to $n_e \sim 6 \times 10^{19}$ m^{-3} the increase in the stored energy does not always mean that the heating has been successfully performed. Therefore, in the shots shown in Fig.7, the mean electron density is carefully controlled so that the same level is obtained at the end of the auxiliary heating(t=270 ms). Figure 7 shows time histories of stored energy obtained from diamagnetism. An increase in the stored energy is observed on every application of a different heating method(ICRF heating in 40 MHz has been reported in the previous paper[24] and is regarded to be an established heating regime along with NBI.). In the comparison of with and without 130 MHz, effectiveness of 130 MHz is shown more convincingly, as a separate phenomenon from the effect of confinement improvement due to the density change.

Figure 8(a) shows an energy spectrum of hydrogen measured with a fast neutral analyzer. When NBI power is applied, high energy hydrogen ion tail is generated for E > 10 keV. The high energy tail is further enhanced when 130 MHz RF power is superposed. This figure suggests that the 3rd harmonics of ion cyclotron damping is a possible mechanism for wave absorption. As predicted by Eq.(4), the presence of high energy ions enhances the wave damping. With a set of parameters adequate for the data set of Fig.8 ($n_e \sim 10\times10^{19}$ m^{-3}, $T_{i,bulk} \sim 1$ keV), the wave damping length due to ions is estimated to be 2.1×10^{4} m and that due to electron Landau damping to be 4.6×10^{5} m. This estimated value of wave damping length by ions may be an overestimate because the wave absorption is further enhanced by the presence of the high energy tail. We notice that wave absorption by ions is larger than wave absorption by electrons; their relation in this heating regime is the reverse of that in the electron heating regime described in section III(a).

On the other hand, the NBI injection does not produce a high energy tail of deuterium since hydrogen beam is used. When 130 MHz RF power is injected, a small high energy deuterium ion tail is generated. However, the tail of the deuterium ion is one order of magnitude smaller in amount than that of the hydrogen ion. The existence of the high energy deuterium ion tail component may be attributed to the 6th harmonics of ion cyclotron damping.

Figure 9 shows the dependence of the stored energy and the neutron yield on the toroidal magnetic field. In the case where

only 40 MHz is applied, the stored energy slightly decreases as the toroidal field increases. This is because the ion cyclotron resonance layer shifts from the plasma center. On the other hand, in the case where both 40 MHz and 130 MHz are applied, the dependence of the stored energy on the toroidal field is weak. The comparison of these curves suggests that the heating efficiency of 130 MHz increases with the strength of toroidal magnetic field compensating for the inverse trend of 40 MHz. We notice also that when only 40 MHz RF is applied the neutron yield decreases as the toroidal field increases. On the other hand, with 130 MHz superposed, the neutron yield increases with increasing toroidal field. These data also indicate a better heating efficiency of 130 MHz at higher toroidal magnetic fields.

Very few experiments have been reported since the importance of controlling k// was proposed[26]. k// spectrum controll was attempted in an experiment to reduce impurity release[26] and, in another application, to change the heating power deposition profile [25,27]. The change of the heating characteristics when antennas are phased still remains a key question. Figure 10 shows the power dependance of the stored energy. The data points are scattered and the dependance on the phase seems to be weak. But, if we focus our attention on the results at a power level of 1 MW, we may see that the phases of $(0,\pi/2,\pi,3\pi/2)$ and $(0,0,0,0)$ are better than the others. Figure 11 shows the power dependance of the radiation power measured with a bolometer. Since the detector views a plasma along the

central chord, its signal reflects the radiation from metal impurities. In planning this experiment, we expected that impurity would be reduced in $(0,\pi,0,\pi)$ phasing . However, as shown in Fig.11, there are no appreciable differences among the different phasing angles. This result is a reproduction of the previous report[25] conducted in two-ion hybrid regime, and different from that of other experiments. This independence of the phasing angle contrasts to the result given in section III(a) where electron heating is atained only with $(0,\pi,0,\pi)$ phasing. This difference is understood in terms of the characteristic of higher harmonic heating; as seen from Eq.(4), the ion cyclotron harmonic term is integrated to lose dependence on $k_{//}$[23]. This is specific to the wave absorption by ions because there exists a resonance layer, though its thickness is small. This is not the case for the electron heating regimes and the exponential term in Eq.(4) shows characteristics in favor of $(0,\pi,0,\pi)$ phasing.

In Fig.12, the efficiency of combined NBI-ICRF-130 MHz heating is compared with that of the NBI-ICRF heating. In this series of experiments the maximum power of 130 MHz is 0.75 MW. In the combined NBI-ICRF-130 MHz heating, we make the total power less than 1.5 MW so that the ratio of $P_{130MHz}/(P_{NBI}+P_{ICRF})$ is larger than unity. The results of high power ICRF heating and its combination with NBI have been reported previously showing that they have reasonable heating efficiencies[24]. In Fig.12, filled circles are the data from the combined heating including

130 MHz, and open circles are those without 130 MHz. We stress here that the 3rd cyclotron harmonic heating has a heating efficiency comparable to established heating methods. This indicates that the 3rd cyclotron harmonic heating may provide a new regime of heating. A merit of using the 3rd cyclotron heating is the potential use of a wave guide antenna. In contrast to the ion Bernstein wave heating case, the wave guide has to be put with the longer side top and bottom in order to give the right polarization. This makes it hard to excite a wave with $k_{//}$ much higher than that of a free wave. Thus, the experimental result that reasonable heating is obtained with shallow phasing angles rather than deep ones is very important.

IV. DISCUSSIONS

The wave absorption profile is calculated using TASK/W1 code (a one-dimensional global wave code)[28]. Figure 13 shows the calculation for the plasma parameter relevant to Fig.2. Here, we assumed $T_e \sim 1.2$ keV. In the calculation of Figs.13(d)-(f), the presence of 2 % 50 keV tail electrons is assumed, while their presence is ignored in Figs.13(a)-(c). The figures (a) and (d) are calculated for (0,0,0,0) phasing, Figs.(b) and (e) are for $(0,\pi/2,\pi,3\pi/2)$ phasing, and Figs.(c) and (f) are for $(0,\pi,0,\pi)$ phasing. It is found from these calculations that in the absence of high energy electron tail, the injected wave ends in wall heating for any phasing angle. It is also found that no significant electron heating is attained for (0,0,0,0) phasing.

This is due to the mismatch of the phase velocity of the wave with the electron thermal velocity. In order for the electron heating mechanism to work sufficiently, the wave $n_{//}$ should be substantially large; this is the case for (e) and (f). This accounts for the fact that electron heating is observed most clearly in $(0,\pi,0,\pi)$ phasing. In the heating regime concerned, the wave produces the high energy tail of electrons with which the wave can interact strongly. However, as the density increases beyond 2×10^{19} m^{-3}, collisional relaxation is enhanced so that high energy tail can no longer be sustained. As briefly studied in section III(a), electron Landau damping dominates in the absence of a high energy tail while transit-time damping dominates when it is present.

The code incorporates the wall loss by assuming a finite conductivity of the wall. However, the use of the resistivity of stainless steel, 5×10^{-7} Ωm, does not bring about any sizable wall loss. The dissipation of the wave energy has long been suspected to actually be much larger than expected theoretically[29]. This is supported in the JIPP T-IIU experiment by the observation of the loading resistance; the wave Q-value of the toroidal eigen mode is not as high as predicted by the theory. Such parasitic dissipation is supposed to be larger than the wave energy absorption by electrons. The parasitic dissipation may be attributed to the strong interaction of the wave with peripheral plasma. The effect is phenomenologically incorporated in Fig.13 by assuming the resistivity of 1×10^{-5} Ωm, which is 20 times the actual value.

From a comparison of Fig.13(a) through (f) with the estimation of damping length shown in section III(a), we get an assessment that wave should be absorbed before they are reflected 10 times in order for a good electron heating to be achieved.

Figure 14 shows the calculated power absorption by hydrogen ions using the same simulation code (TASK/W1 code). The parameters are chosen so that the result can be directly compared with the ion heating regime described in section III(b). Without hydrogen tail(Figs.14(a) ~ (c)), most of the wave energy ends in the wall loss and the remaining portion is absorbed through electron Landau damping. The wave absorption at the ion cyclotron resonance layer is small. On the other hand, with a hydrogen tail(Fig.14(d) ~ (f)), a greater portion of the injected RF power is absorbed by the hydrogen tail at the ion cyclotron resonance layer. This is a characteristic of higher harmonic heating due to the finite Larmor radius effect. The experimental fact that 3rd cyclotron harmonic heating is clearly achieved in combination with other heating is naturally accounted for by this mechanism. It is also noted in Fig.14 that the wave absorption by ions is not as much influenced by phasing angles as is that by electrons.

Figure 15 shows the B_t dependence of the power absorbed by the hydrogen tail calculated using the same simulation code. The scattering of the data reflects the presence of the toroidal eigen mode. The shaded region represents the range where B_t is scanned in the experiment. Within this region, the layer of the 3rd harmonics of ion cyclotron resonance approaches the plasma center as B_t is raised, and the wave energy absorbed by ions

increases correspondingly. This agrees with the experimental result that the stored energy and neutron yield increase with increasing B_t. The calculation code also incorporates wave absorption by deuterium ions at the layer of 5, 6, and 7ω_{cD}. However, because of the higher order of the harmonics, this absorption mechanism is predicted to be small.

V. CONCLUSION

It was shown experimentally that there are two heating mechanisms competing with each other in the intermediate range of frequency: electron heating dominates in the low density regime where small power input is enough to distort the electron distribution function. This, in turn, resolves the so-called spectrum gap problem which is more serious in FWCD than in LHCD. The electron heating was observed most clearly in $(0,\pi,0,\pi)$ phasing which allows for the wave launching at the maximum possible parallel wave number. The electron heating was recorded up to a density of 2×10^{19} m^{-3}, which is higher than the predicted LHCD density limit by two orders of magnitude. An analysis using a global wave code shows a reasonably strong wave absorption in the presence of slide-away electrons which are observed in the experiment.

Ions are heated in the high density regime. When 130 MHz is combined with NBI and/or ICRF(40 MHz two-ion hybrid) heating, a particularly high heating efficiency is obtained. When 130 MHz is applied, the growth of the hydrogen high energy tail is observed. From this it is inferred that the heating mechanism is

3rd ion cyclotron harmonic damping. This conclusion is also supported by the fact that the neutron yield increases as the 3rd cyclotron resonance layer is shifted toward the central chord when B_t is varied.

A merit of using a high frequency for heating is also in the possible use of wave guide antennas. The generation of a high energy tail may be useful in enhancing thermonuclear fusion Q-value in the start-up phase of a reactor.

The simulation code predict that the presence of the high energy tail enhances the wave absorption by ions and makes it dominate in the experiment over the wall loss and electron heating. This is a characteristic of general higher harmonic cyclotron damping which is based on the finite Larmor radius effect. The experiment also showed that ion heating is less sensitive to the phasing angle than electron heating as predicted by the theory.

REFERENCES

[1] WEGROWE,J.G., ENGELMANN,F., Comments Plasma Phys. Controlled Fusion 8 (1984) 211

[2] SVERDRUP,L.H., BELLAN,P.M., Phys. Rev. Lett. 59 (1987) 1197

[3] WONG,K.L., ONO,M., Nucl. Fusion 23 (1983) 805

[4] EHST,D.A., in Non-inductive Current drive in Tokamaks (Proc. IAEA Technical Committee Meeting Culham, 1983) Vol.2 (1983) 442

[5] MOREAU,D., JACQUINOT,J., LALLIA,P.P., in Controlled Fusion and Plasma Heating (Proc. 13th Eur. Conf. Schliersee, 1986), Vol.10C, Part II, European Physical Society (1986) 421

[6] EHST,D.A., Argonne National Laboratory Report ANL/FPP/TM-219, 1988

[7] ANDREWS,P.L., BHADRA,D.K., Nucl. Fusion 26 (1986) 897

[8] CHIU,S.C., CHAN,V.S., HARVEY,R.W., PORKOLAB,M., Nucl. Fusion 29 (1989) 2175

[9] MAU,T.K., in Radio-Frequency Power in Plasmas (Proc. 8th Topical Conf. Irvine, 1989), AIP, New York (1989) 158

[10] ANDO,R., KAKO,E., OGAWA,Y., WATARI,T., Nucl. Fusion 26 (1986) 1619

[11] OHKUBO,K., HAMADA,Y., OGAWA,Y., et al., Phys. Rev. Lett. 56 (1986) 2040

[12] OHKUBO,K., MATSUMOTO,K., Jpn. J. Appl. Phys. 26 (1987) 142

[13] TOI,K., HAMADA,Y., OHKUBO,K., et al., IPPJ-828 (Fast Wave Injection into High Temperature Tokamak Plasma in the Lower Hybrid-Density Regime of JIPP T-IIU), or WATARI,T., OHKUBO,K., AKIYAMA,R., et al., in Plasma

Physics and Controlled Nuclear Fusion Research 1986 (Proc. 11th Int. Conf. Kyoto ,1986), Vol.1, IAEA, Vienna (1987) 495

[14] TAKASE,Y., WATARI,T., KUMAZAWA,R., et al., NIFS 21

[15] GOREE,J., ONO,M., COLESTOCK,P., HORTON,R., McNEEL,D., PARK,H., Phys. Rev. Lett. 55 (1985) 1669

[16] YAMAMOTO,T., Phys. Rev. Lett. 11 (1989) 1148

[17] PINSKER,R.I., COLESTOCK,P.L., BERNABEI,S., et al., in Radio-Frequency Power to Plasmas (Proc. 7th Topical Conf. Kissimmee, 1987), American Physical Society (1987) 175

[18] UESUGI,Y., YAMAMOTO,T., KAWASHIMA,H., et al., Nucl. Fusion 30 (1990) 297

[19] HOSEA,J., BRETZ, N., CAVALLO, A., et al., in Heating in Toroidal Plasmas (Proc. 3rd Int. Symp. Grenoble, 1982), Vol.I (1982) 213

[20] ODAJIMA,K., MATSUMOTO, H., KIMURA, H., et al., in Heating in Toroidal Plasmas (Proc. 4th Int. Symp. Roma, 1984), Vol.I (1984) 243

[21] STEINMETZ,K., FUSSMANN, G., GRUBER, O., et al., Plasma Physics and Controlled Fusion 28 (1986) 235

[22] FUJII,T., KIMURA,H., SAIGUSA,M., et al., in Controlled Fusion and Plasma Heating (Proc. 15th Eur. Conf. Dubrovnik, 1988), Vol.12B, Part II, European Physical Society (1988) 766

[23] STIX,T.H., Nucl. Fusion 15 (1975) 737

[24] WATARI,T., KUMAZAWA,R., TOI,K., et al., Nucl. Fusion 30 (1990) 1197

[25] ANDO,R., SATO,K., WATARI,T., et al., Nucl. Fusion 28 (1988)

577

[26] TAMAI,H., ODAJIMA,K., MATSUMOTO,H., et al, Nucl. Fusion 26 (1986) 365

[27] JACQUINOT,J., ANDERSON,R.J., ARBEZ,J., et al., Plasma Physics and Controlled Fusion 28 (1986) 1

[28] FUKUYAMA,A., NISHIYAMA,S., ITOH,K., ITOH,S.-I., Nucl. Fusion 23 (1983) 1005

[29] TAKAHASHI,H., J. de Phys. Paris, Colloq. C6 38 (1977) 171

FIGURE CAPTIONS

Fig.1. JIPP T-IIU tokamak: the toroidal locations of 130 MHz RF antenna array, ICRF(40 MHz) antennas, and NBI injector are shown. The diagnostics used in the experiment are also shown.

Fig.2. Time history of the typical shot: (a); ECE signal of central chord and 130 MHz RF power, (b); stored energy obtained from diamagnetic signal and flux measurement, (c); plasma density and internal inductance l_i, (d); P_{Ohm}: the broken line is without dl_i/dt correction and the solid line is with full correction.

Fig.3. The soft X-ray energy spectrum: the solid line; with 130 MHz, and the broken line; without 130 MHz. The experimental conditions are the same as for the shots shown in Fig.2.

Fig.4. The density dependence of the stored energy. Filled circles are data points without 130 MHz showing an Alcator type dependence. Open circles are those with 130 MHz. The difference between them is the net increment due to applying 130 MHz.

Fig.5. The experimental conditions of various fast wave experiments.

Fig.6. Time history of the typical shot. (a); plasma current and loop voltage, (b); P_{Ohm}, P_{NBI}, P_{ICRF}, and $P_{130\ MHz}$, (c); mean electron density and neutron yield, (d); central electron temperature and $H\alpha$ signal of central chord, (e); stored energy measured with diamagnetism.

Fig.7. Time history of stored energy measured with diamagnetism. Comparison is made between the shots with and without 130MHz, ie., NBI + ICRF(40 MHz) and NBI +ICRF(40 MHz) +130MHz RF heating.

Fig.8. (a); energy spectrum of hydrogen measured with fast neutral analyzer. Open circles are the data with only NBI and filled circles are the data with NBI + 130 MHz. (b); energy spectrum of deuterium. Open and filled circles are with NBI only and NBI + 130 MHz, respectively.

Fig.9. (a); the dependence of stored energy on toroidal magnetic field. Open circles show the case where only 40 MHz is applied to plasma. Solid circles show the case where 130 MHz is applied to plasma in addition to 40 MHz. (b); the dependance of neutron yield on toroidal magnetic field. Solid and open circles are with and without 130 MHz, respectively.

Fig.10. The power dependance of stored energy in various antenna phasings: open circles; $(0,\pi,0,\pi)$, squares; $(0,0,0,0)$, filled circles; $(0,\pi/2,\pi,3\pi/2)$, and triangles; $(0,-\pi/2,-\pi,-3\pi/2)$.Total power refers to the sum of 130MHz RF power, 40 MHz RF power, and NBI power(300 kW).
The mean electron density is $(6\sim7)\times10^{19}m^{-3}$.

Fig.11. The power dependance of radiation loss measured with bolometer. The symbols are the same as those in

Fig.10. The mean electron density is $(6\sim7)\times10^{19}$ m^{-3}.

Fig.12. A comparison of heating efficiency between the present experiment and the heating experiment in 1988. Open circles are the data from the 1988 experiment (conventional heating; 40 MHz and NBI heating). Filled circles are the data from present experiment with 130 MHz.

Fig.13. The power deposition profile calculated for the electron heating case using the TASK/W1 code. The plasma parameters are $n_e = 3\times10^{19}$ m^{-3}, $T_e = 1.2$ keV, and $T_i = 0.4$ keV. A deuterium plasma of 10 % hydrogen minority is assumed. The left row, (a)-(c), are calculations without a high energy electron tail. The right row, (d)-(f), are calculations with a high energy tail of 50 keV and 2 % in amount. Broken lines indicate the power absorbed by the bulk electrons, the chain dotted line indicates that absorbed by the high energy electron tail, the solid line indicates that absorbed by the hydrogen ions. Wave energy flux is also shown by the solid line, the intensity of which decreases as it passes across the plasma cross section. The ordinate on the left is the power density in the unit of MW/m and that on the right is the wave energy flux in the unit of MW(note that the calculation is one-dimensional).

Fig.14. The power deposition profile calculated for the ion heating case using TASK/W1 code. Central

electron density is 1.05×10^{20} m^{-3} and a deuterium plasma of 10 % hydrogen minority is assumed. Central electron temperature is 1.2 keV and central ion temperature is 0.4 keV. The figures in the left row, (a)-(c), are without a hydrogen tail, while the figures in the right row, (d)-(f), include a 1 % - 5 keV hydrogen tail. Representation of lines and coordinates are the same as in Fig.13.

Fig.15. The calculated B_t dependence of the power absorption by ions. The shaded region(B_t ~ 2.75 - 3.0 T) is the range to be compared with the experiment.

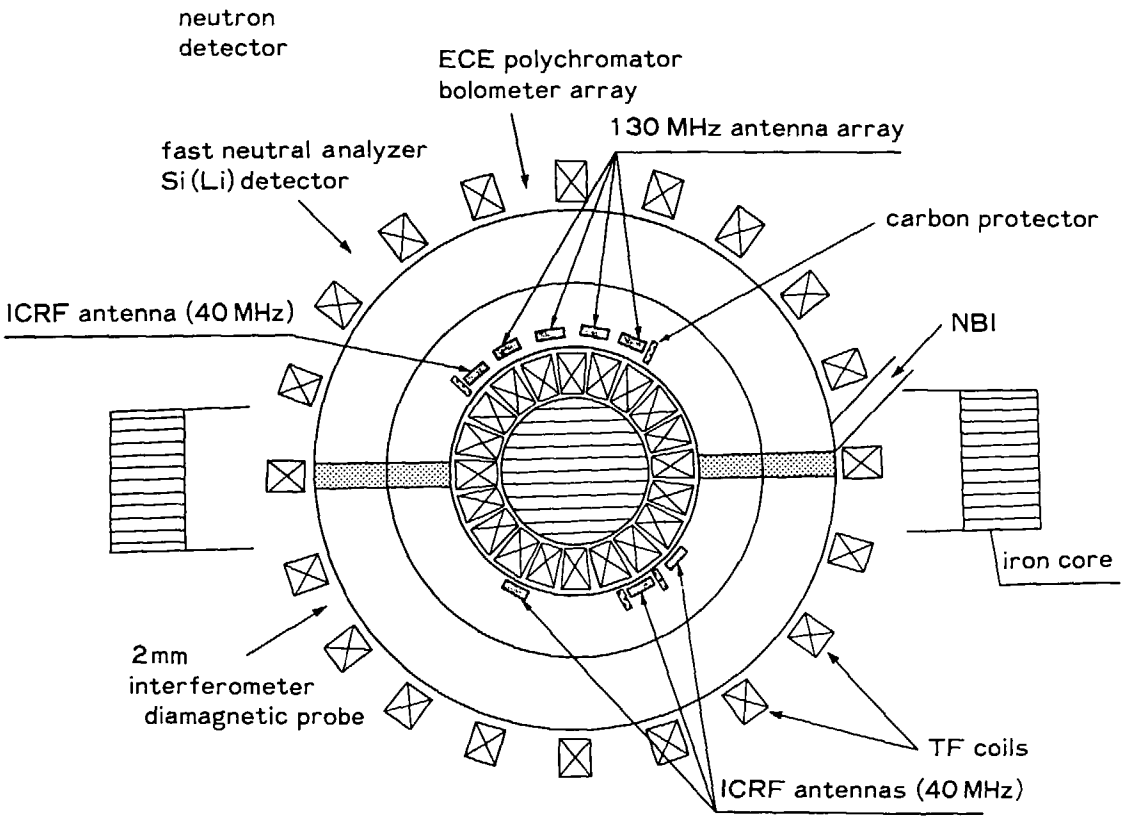
neutron
detector
ECE polychromator
bolometer array
130 MHz antenna array
fast neutral analyzer
Si (Li) detector
carbon protector
ICRF antenna (40 MHz)
NBI
iron core
2mm
interferometer
diamagnetic probe
TF coils
ICRF antennas (40 MHz)

Fig.1

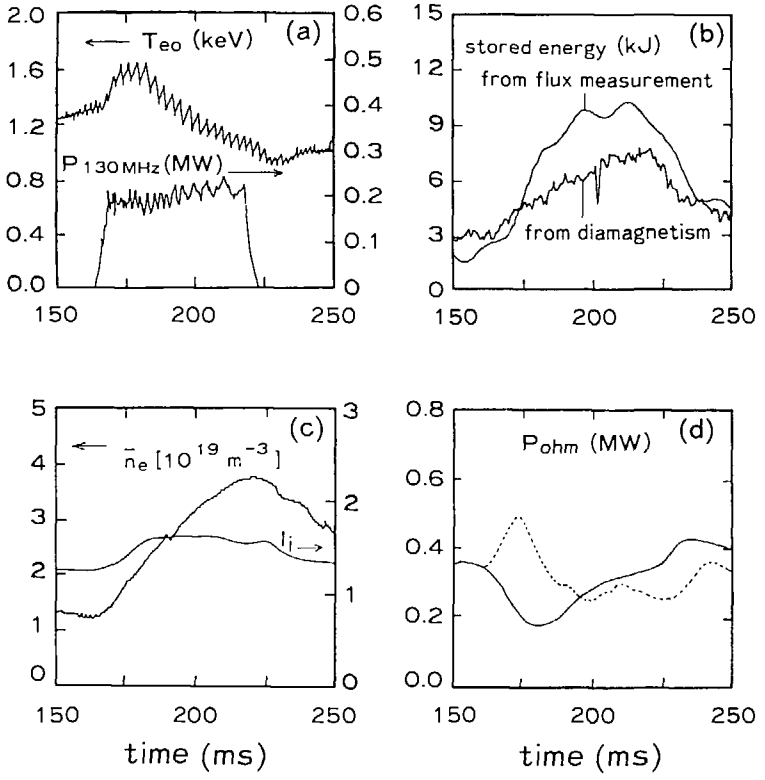
(a)
← Teo (keV)
P 130 MHz (MW)
(b)
stored energy (kJ)
from flux measurement
from diamagnetism
(c)
← ne [10^19 m^-3]
li →
(d)
Pohm (MW)
time (ms)
time (ms)

Fig.2

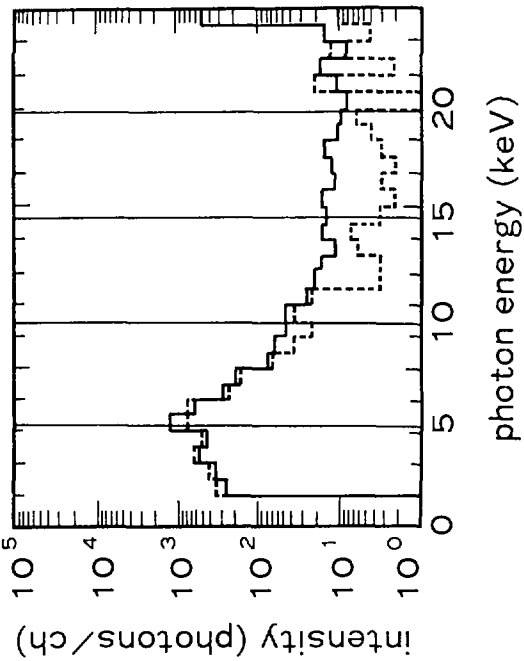
intensity (photons/ch)
10^5
10^4
10^3
10^2
10^1
10^0
0
5
10
15
20
photon energy (keV)

Fig.3

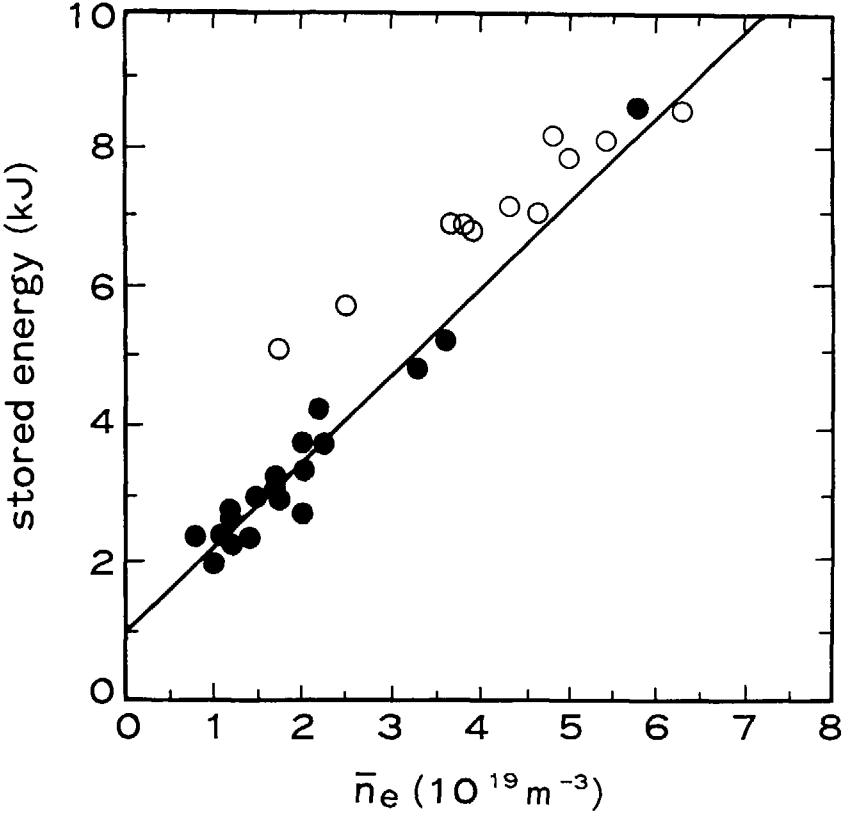

Fig.4

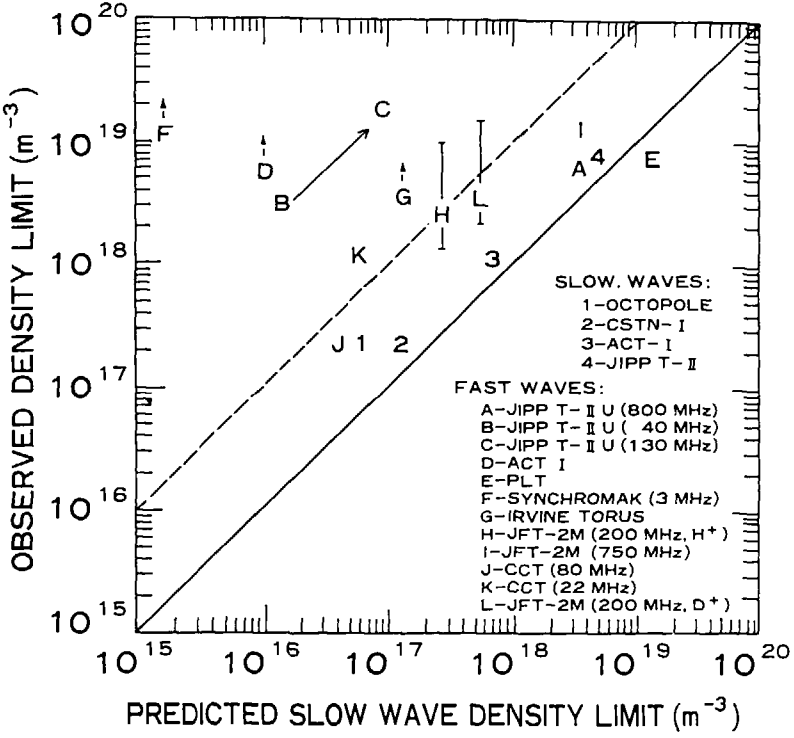
OBSERVED DENSITY LIMIT (m^{-3})
PREDICTED SLOW WAVE DENSITY LIMIT (m^{-3})
10^{15}
10^{16}
10^{17}
10^{18}
10^{19}
10^{20}
SLOW. WAVES:
1-OCTOPOLE
2-CSTN-I
3-ACT-I
4-JIPP T-II
FAST WAVES:
A-JIPP T-II U (800 MHz)
B-JIPP T-II U (40 MHz)
C-JIPP T-II U (130 MHz)
D-ACT I
E-PLT
F-SYNCHROMAK (3 MHz)
G-IRVINE TORUS
H-JFT-2M (200 MHz, H^+)
I-JFT-2M (750 MHz)
J-CCT (80 MHz)
K-CCT (22 MHz)
L-JFT-2M (200 MHz, D^+)

Fig. 5

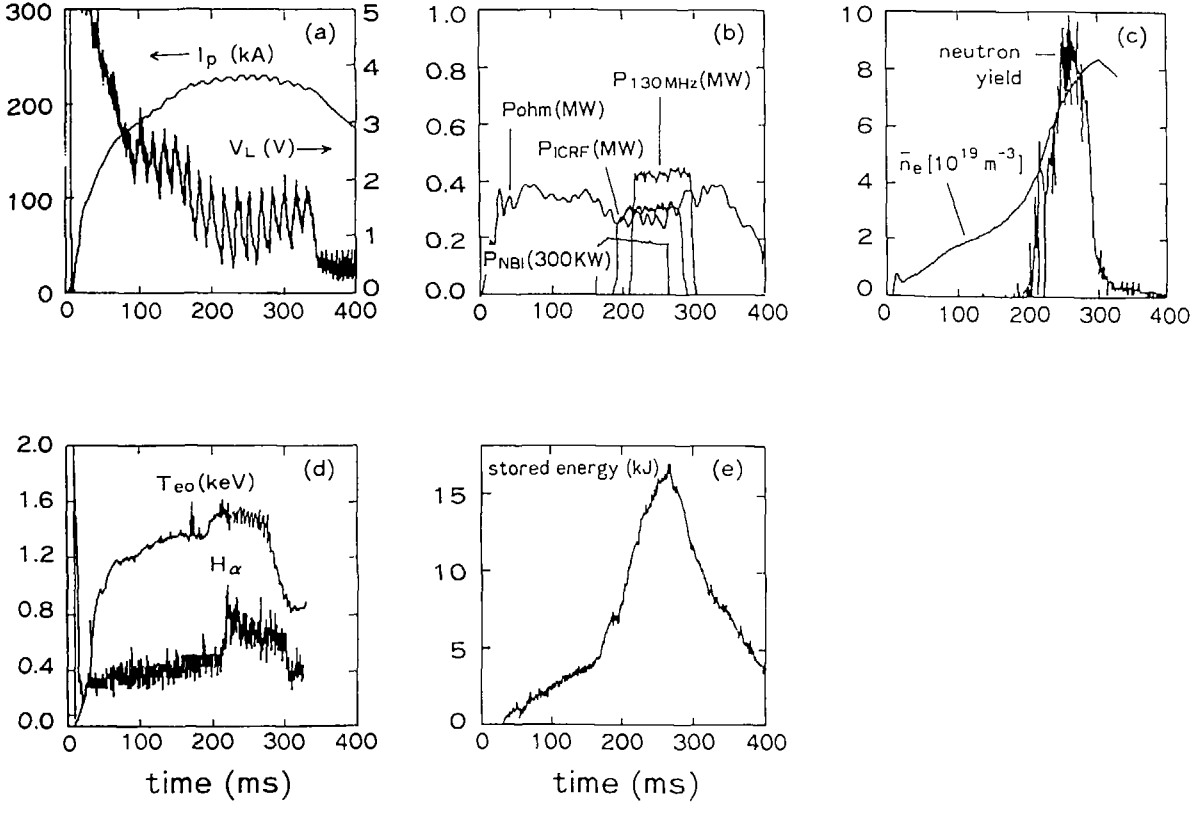
(a)
I_p (kA)
V_L (V)
(b)
Pohm(MW)
P_{ICRF}(MW)
P_{130MHz}(MW)
P_{NBI}(300KW)
(c)
neutron yield
$\bar{n}_e[10^{19}\,m^{-3}]$
(d)
T_{eo}(keV)
H_α
time (ms)
(e)
stored energy (kJ)
time (ms)

Fig.6

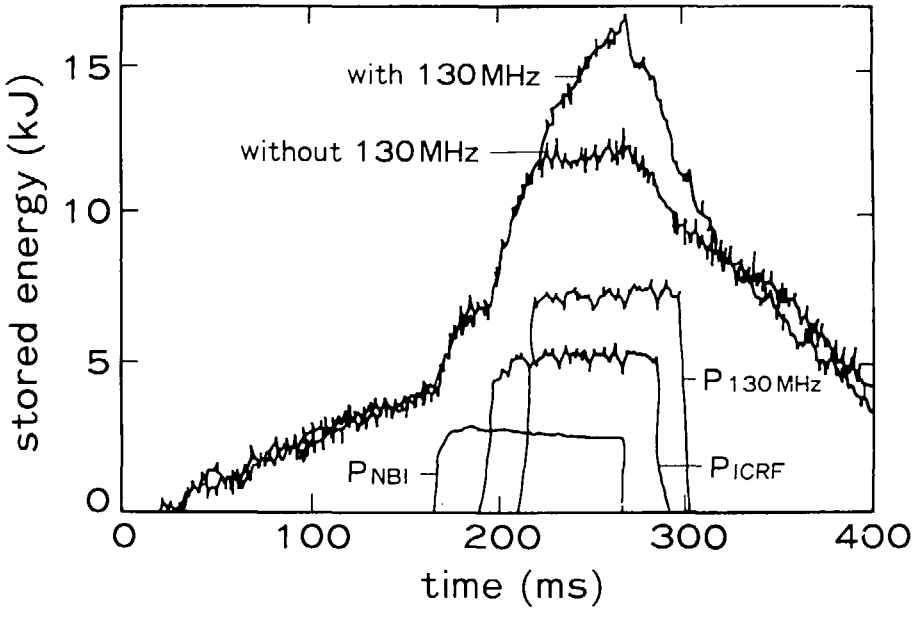
stored energy (kJ)
15
10
5
0
0
100
200
300
400
time (ms)
with 130MHz
without 130MHz
P 130MHz
P NBI
P ICRF

Fig.7

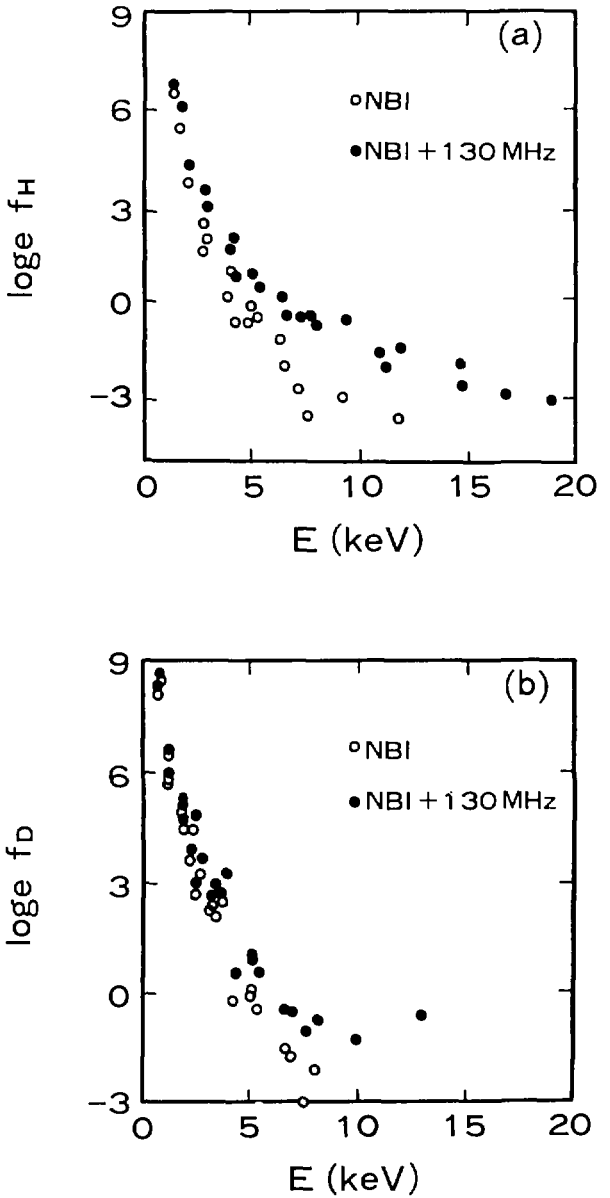

Fig.8

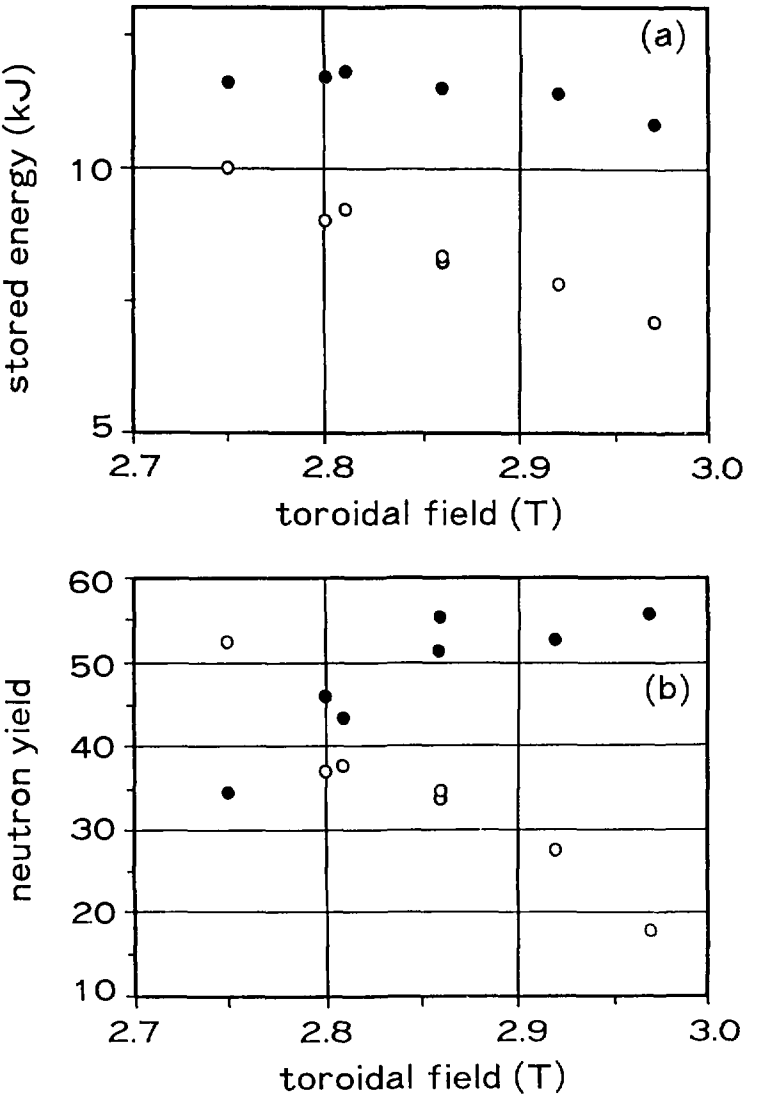
(a)
stored energy (kJ)
10
5
2.7
2.8
2.9
3.0
toroidal field (T)
(b)
neutron yield
60
50
40
30
20
10
2.7
2.8
2.9
3.0
toroidal field (T)

Fig.9

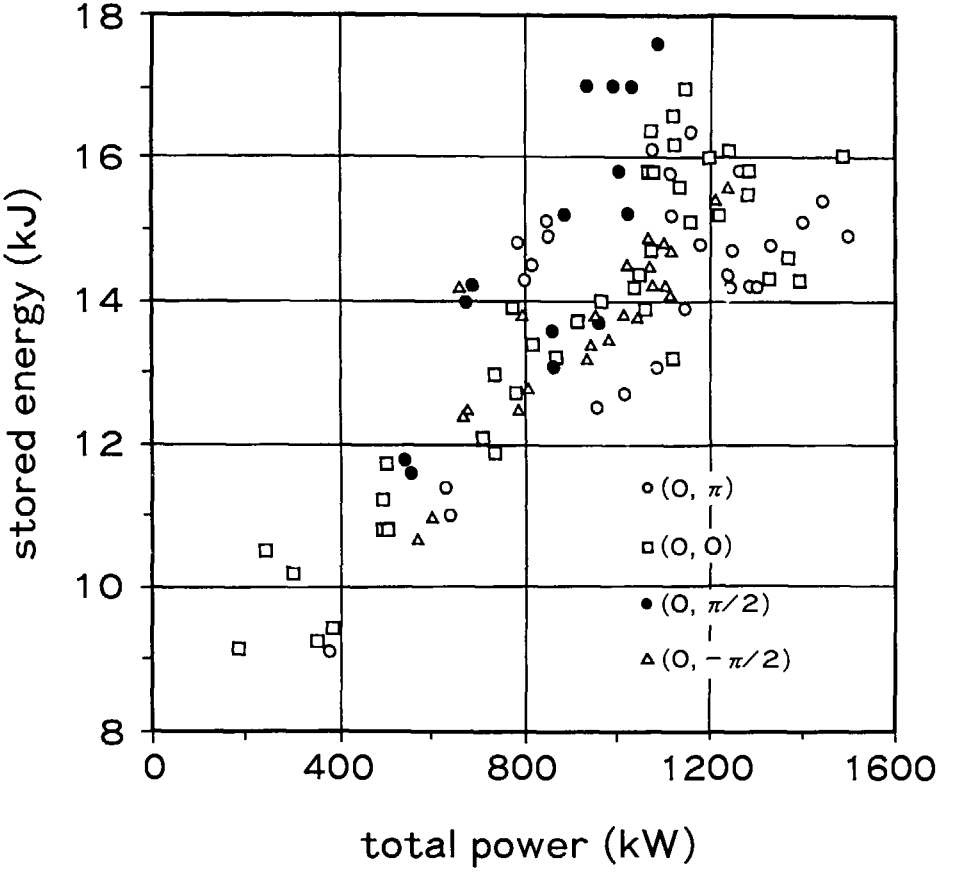
stored energy (kJ)
18
16
14
12
10
8
0
400
800
1200
1600
total power (kW)
(0, π)
(0, 0)
(0, π/2)
(0, −π/2)

Fig.10

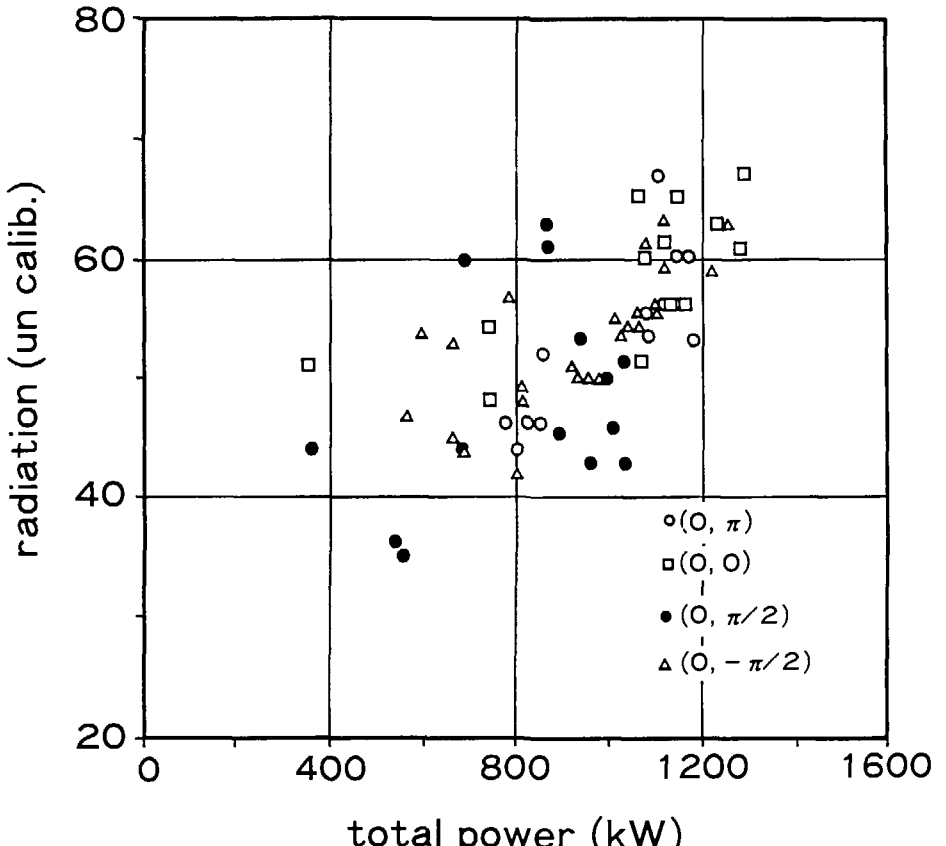
80
60
40
20
0
400
800
1200
1600
radiation (un calib.)
total power (kW)
○(0, π)
□(0, 0)
●(0, π/2)
△(0, −π/2)

Fig.11

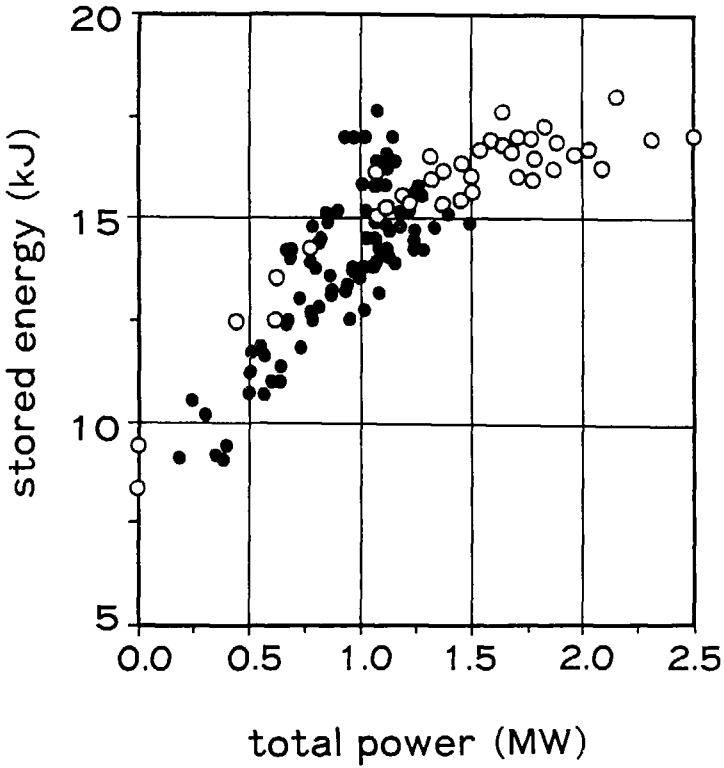

Fig.12

power density [MW/m]
(a)
(0, 0, 0, 0)
(b)
$(0, \frac{\pi}{2}, \pi, \frac{3}{2}\pi)$
(c)
$(0, \pi, 0, \pi)$
wave energy flux [MW]
position[m]
power density [MW/m]
(d)
(0, 0, 0, 0)
(e)
$(0, \frac{\pi}{2}, \pi, \frac{3}{2}\pi)$
(f)
$(0, \pi, 0, \pi)$
wave energy flux [MW]
position [m]

Fig.13

power density [MW/m]
(a)
(0, 0, 0, 0)
(b)
(0, π/2, π, 3/2 π)
(c)
(0, π, 0, π)
wave energy flux [MW]
position [m]
power density [MW/m]
(d)
(0, 0, 0, 0)
(e)
(0, π/2, π, 3/2 π)
(f)
(0, π, 0, π)
wave energy flux [MW]
position [m]

Fig.14

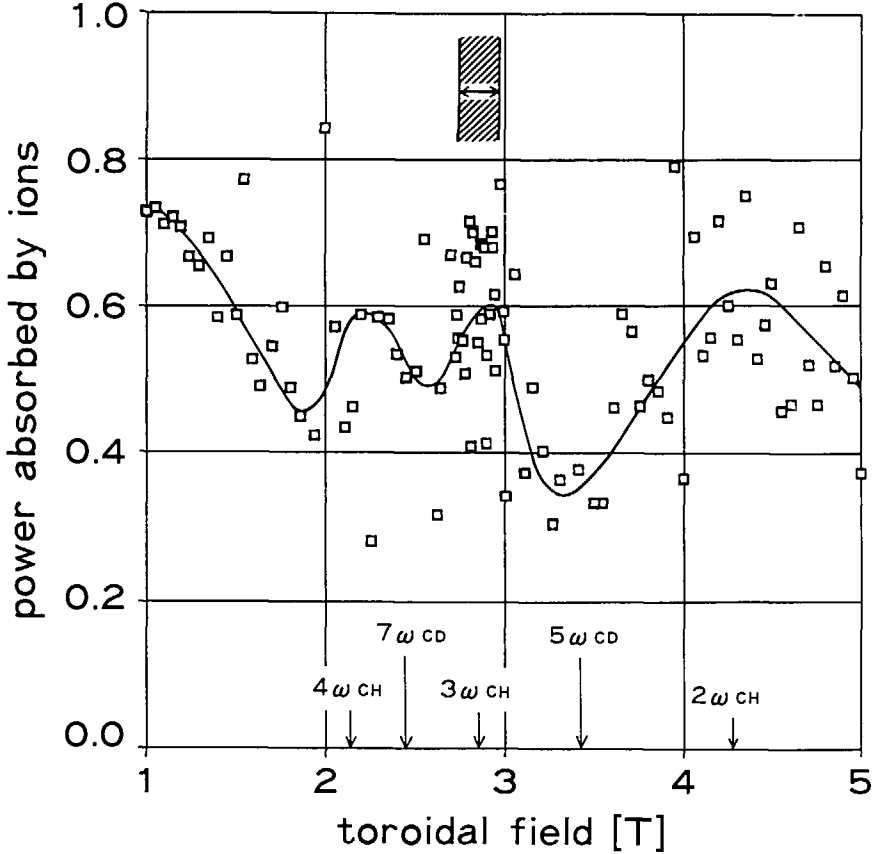
power absorbed by ions
1.0
0.8
0.6
0.4
0.2
0.0
1
2
3
4
5
toroidal field [T]
7ω CD
5ω CD
4ω CH
3ω CH
2ω CH

Fig.15